npj | Computational Materials

www.nature.com/npjcompumats

ARTICLE OPEN

Enhancing hydrogen evolution on the basal plane of transition metal dichacolgenide van der Waals heterostructures

Faling Ling[1], Wei Kang[1], Huirong Jing[1], Wen Zeng[1], Yankun Chen[1], Xiaoqing Liu[1], Yixin Zhang[1], Lin Qi[1], Liang Fang[2] and Miao Zhou[1]

Recent years have seen a surge in the use of low-dimensional transition metal dichacolgenides, such as MoS_2, as catalysts for the electrochemical hydrogen evolution reaction. In particular, sulfur vacancies in MoS_2 can activate the inert basal plane, but that requires an unrealistically high defect concentration (~9%) to achieve optimal activity. In this work, we demonstrate by first-principles calculations that assembling van der Waals heterostructures can enhance the catalytic activity of MoS_2 with low concentrations of sulfur vacancies. We integrate MoS_2 with various two-dimensional nanostructures, including graphene, *h*-BN, phosphorene, transition metal dichacolgenides, MXenes, and their derivatives, aiming to fine-tune the free energy of atomic hydrogen adsorption. Remarkably, an optimal free energy can be achieved for a low sulfur vacancy concentration of ~2.5% in the MoS_2/MXene-OH heterostructure, as well as high porosity and tunability. These results demonstrate the potential of combining two-dimensional van der Waals assembly with defect engineering for efficient hydrogen production.

npj Computational Materials (2019)5:20 ; https://doi.org/10.1038/s41524-019-0161-8

INTRODUCTION

Owing to their low cost, earth abundance and high activity, transition metal dichacolgenides (TMDs), such as MoS_2, have become a promising alternative to platinum (Pt) for catalyzing hydrogen (H_2) production from water in the last decade.[1–3] It was demonstrated that edges of MoS_2 are active sites for hydrogen evolution reaction (HER),[4–6] and plenty of strategies have been developed to enhance the catalytic activity either by maximizing the exposed edge sites through synthesis of nanostructures,[7–11] or by increasing the intrinsic activity of MoS_2 through electronic structure modifications *via* chemical doping or using strain.[12–15] To increase the overall catalytic performance, it is highly desirable to utilize the basal plane of MoS_2 because it provides the most possible active sites towards HER. Despite the chemical inertness of pristine surface, tremendous efforts have been devoted to activating the basal plane of two-dimensional (2D) MoS_2. As an example, phase transition from semiconducting 2H to metallic 1T/1T′ phase dramatically enhances the catalytic activity of MoS_2.[16–18] However, the 1T/1T′ phase of MoS_2 is metastable and would be transformed to the more stable 2H phase under irradiation or mild heating conditions,[19,20] severely limiting its practical applications.

Recently, both theoretical and experimental studies showed that the inert basal plane of MoS_2 can be activated by creating sulfur vacancy (V_S).[21–24] In particular, Hong et al. presented a detailed study on point defects in 2D MoS_2 and found that V_S is the most energy-favorable defect on the basal plane.[23] Li et al. explored the catalytic properties of various active sites in MoS_2, and found that V_S on the basal plane provides one major active site for HER in addition to edges.[24] Interestingly, it was experimentally shown that the catalytic performance strongly depends on the concentration of V_S (V_S%), for which an optimal HER activity can only be achieved when V_S% reaches ~9%. However, MoS_2 prepared by approaches of mechanical exfoliation, physical or chemical vapor deposition has a typical V_S% of 1~5%,[23,25,26] far below the concentration needed for high activity. Controlled argon or oxygen plasma exposure can produce higher V_S%, but they require high vacuum and sophisticated experimental procedures, which is undesirable for large-scale synthesis.[24,27] More importantly, MoS_2 with high V_S% will have high surface energy, which weakens the structural stability and severely limits the operating lifetime.[28] Therefore, to find an effective and practical way to enhance the catalytic activity of MoS_2 basal plane with low V_S% becomes a key issue for future development of high-performance catalyst for efficient H_2 production.

Normally, hydrogen evolution proceeds *via* either the Volmer-Heyrovsky or the Volmer-Tafel reaction pathway, with both pathways involving one rate-limiting step, known as the chemisorption of atomic H intermediate on catalyst surface.[29] High-performance catalyst should adsorb H neither too weak nor too strong, i.e., the Gibbs free energy of H adsorption (ΔG_H) is close to zero.[30] V_S on the basal plane modifies the electronic structures of MoS_2 by introducing defect states inside the semiconducting gap of pristine MoS_2, which hold responsibility for H adsorption.[15,28] In this endeavor, controlling the electronic properties of V_S rather than increasing its concentration would be more effective and practical to optimize the catalytic performance.

Recent advances in van der Waals heterostructures have invoked substantial interest in tailoring the electronic properties of 2D structures through interfacial coupling.[31,32] It was shown that by combination of different materials to form heterostructures, novel physical phenomena and electronic behaviors arise that cannot be derived from their constituent layers.[33,34] In particular, as catalyst for HER, Liu et al. synthesized 1T phase of MoS_2 on flexible single-walled carbon nanotube (SWNT) and found that MoS_2/SWNT composite exhibits increased activity.[35]

[1]Key Laboratory of Optoelectronic Technology and System of Ministry of Education, College of Optoelectronic Engineering, Chongqing University, Chongqing 400044, P. R. China and [2]College of Physics, Chongqing University, Chongqing 400044, P. R. China
Correspondence: Miao Zhou (mzhou@cqu.edu.cn)

Received: 20 October 2018 Accepted: 25 January 2019
Published online: 18 February 2019

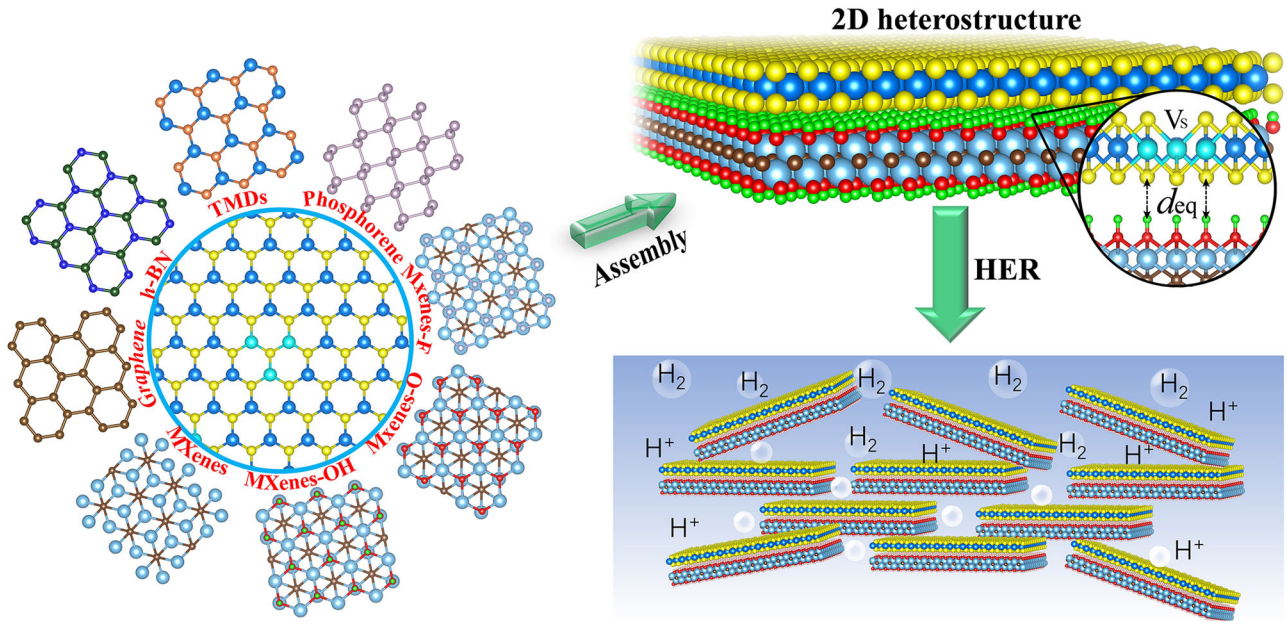

Fig. 1 A schematic description of assembling 2D van der Waals heterostructures by combining MoS_2 and various 2D structures as porous catalyst for HER. The equilibrium distance (d_{eq}) between MoS_2 with V_S and 2D structure is highlighted

Similar findings were also reported in MoS_2/phosphorus and MoS_2/$CoSe_2$ heterostructures for HER.[36,37] Despite these studies, however, the operating performance of MoS_2-based catalyst remains to be improved, which requires not only a deep understanding of the physical mechanism associated with electronic structures, but also the optimization of interfacial interaction by synthesizing appropriate heterostructures/composites.

In this work, aiming to optimize the interfacial interaction and enhance the catalytic capability of MoS_2, by means of first-principles calculations based on density functional theory (DFT), we investigated a variety of van der Waals heterostructures constructed by assembling MoS_2 with other common 2D structures (see Fig. 1), including graphene, *h*-BN, black phosphorene, TMDs (MoS_2, WS_2 and $MoSe_2$) and transition metal carbides/nitrides (Ti_2C, Ti_3C_2, V_2C and Ti_2N) that are also termed as MXenes. In experiment, MXenes are often terminated with functional groups, such as –OH, –O, and –F.[38] Therefore, we also considered the functionalized derivatives of MXene, MXene-X (X = OH, O, F). Systematic studies on the adsorption of atomic H on V_S with different concentrations reveal that characteristics of V_S-induced defect states, especially the position and density of the lowest unoccupied state, can be fine-tuned by interlayer interaction within the heterostructure. Most remarkably, we found that with MoS_2/MXene-OH heterostructure, an optimal H adsorption with $\Delta G_H = 0$ eV can be realized at an unprecedented low V_S% of 2.5%, which is readily achievable in practice. Moreover, the layered geometry within such heterostructures bears advantages of maximized active V_S exposure for efficient catalyst with high porosity (see Fig. 1), paving an interesting avenue for practical implementation. These findings are generally applicable, which may shed new light on future exploration and development of heterogeneous catalysts based on van der Waals heterostructures for HER and other important chemical reactions.

RESULTS AND DISCUSSION

Before studying 2D heterostructures, we first investigated the relationship between concentration of V_S on MoS_2 and the catalytic activity towards HER. Figure 2a shows the optimized structure of atomic H adsorption at V_S site on the basal plane of freestanding MoS_2. On pristine MoS_2 (V_S% = 0.00%), ΔG_H was calculated to be over 2 eV (endothermal), indicating that the pristine basal plane of MoS_2 is indeed chemically inert, in agreement with previous reports.[39] When 1.56% of V_S was introduced, H becomes much easier to be adsorbed on the exposed Mo atom, with ΔG_H greatly decreased to 0.226 eV. As V_S% increases (detailed structures are presented in Fig. S1 in Supplementary Information), ΔG_H further reduces and approaches 0 eV when V_S% reaches a critical value within a range of 7.81~9.38% (Fig. 2b and S2). These findings are consistent with available experimental observations.[24]

Figure 2c displays the electronic structures of MoS_2 with different concentrations of V_S. As H is adsorbed on the exposed Mo atom, we focus on partial density of states (PDOS) projected onto Mo *d* orbitals with which H *s* orbital interacts. For pristine TMDs, previous studies indicated that the lowest unoccupied state, especially the state located below normal hydrogen electrode potential (V_{NHE} = -4.5 eV *vs.* vacuum level), plays a decisive role in the determination of atomic H adsorption.[40,41] Here, our calculations show that pristine MoS_2 has available empty states located above the conduction band minimum (CBM), much higher than V_{NHE}, thus leading to an unfavorable adsorption. With the presence of V_S, defect states arise inside the energy gap of MoS_2, which are unfilled and located below –4.5 eV so that electron of atomic H can fill in. This results in increased adsorption strength of H. With increasing V_S%, more defect states appear and become closer to V_{NHE}, and a gradual upshift of valence bands can be observed (note that we have aligned all energies to the vacuum level). Clearly, characteristics of the V_S-induced defect states, especially the position and density of the lowest unoccupied state, determine the adsorption strength of atomic H. This may also provide an efficient descriptor of HER on the basal plane of MoS_2.

Next, we turn to explore the van der Waals heterostructures constructed by assembly of MoS_2 with one V_S and other 2D materials. In literature, heterostructures including MoS_2/graphene,[42–44] MoS_2/*h*-BN,[45,46] MoS_2/black phosphorus[36,47] and bilayer sheets of TMDs (MoS_2/WS_2 and MoS_2/$MoSe_2$)[48,49] have been successfully fabricated for batteries, supercapacitors and photodevices. Novel semiconductor/metal contact was also theoretically proposed by matching MoS_2 with MXenes and their

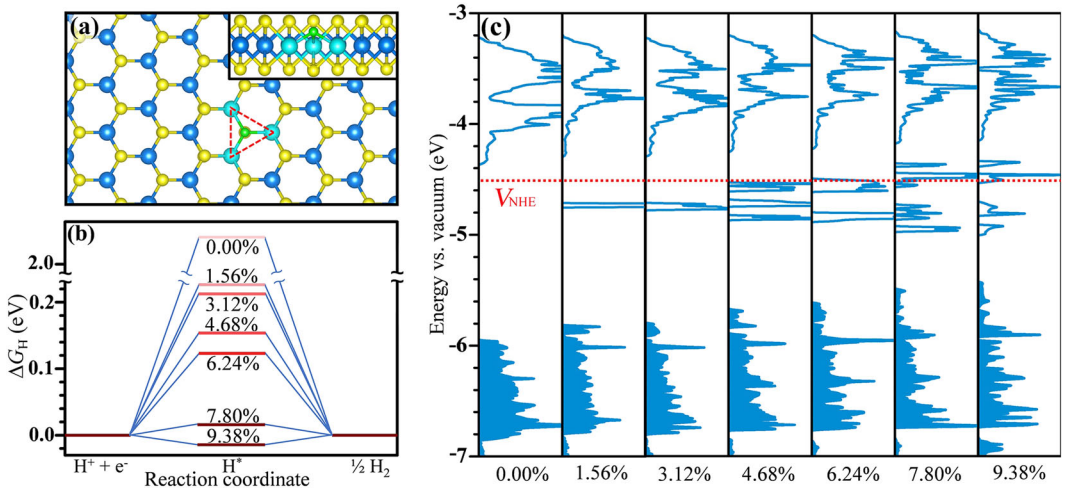

Fig. 2 **a** Optimized structure of atomic H adsorption on V_S of 2D MoS_2. Inset shows the side view. Saturated (exposed) Mo atoms are shown in dark (light) blue, S atoms in orange and H in green. **b** ΔG_H against the reaction coordinate of HER with different V_S%. H^* refers to atomic H adsorbed at V_S. **c** PDOS projected onto Mo *d* orbitals of the adsorbed systems with different V_S%. Filled and empty areas denote the occupied and unoccupied states, respectively. Energy location of V_{NHE} (–4.5 eV *vs.* vacuum level) is denoted as the red dashed line

Table 1. Lattice mismatch between MoS_2 and other 2D structures (negative value suggests compressing the 2D structure and positive means stretching the structure), the calculated equilibrium distance (d_{eq}), binding energy (E_b) and work function (W_F) of isolated 2D structures

Material	Mismatch	d_{eq} (Å)	E_b (eV/Mo)	W_F (eV)
Graphene	4.20%	3.47	0.18	4.5
h-BN	2.00%	3.48	0.18	3.7
Phosphorene	−2.70%	3.38	0.20	4.7
MoS_2	0.00%	3.21	0.20	5.2
WS_2	0.00%	3.23	0.20	4.8
$MoSe_2$	−4.00%	3.29	0.20	4.1
Ti_2C	4.10%	1.67	1.67	4.5
Ti_2C-OH	3.42%	2.35	0.40	1.6
Ti_2C-O	4.00%	2.90	0.20	5.6
Ti_2C-F	2.80%	2.80	0.19	5.3

derivatives.[50] Here, we screened various 2D materials and selected a total of 16 representative structures, including graphene, *h*-BN, black phosphorene, TMDs (MoS_2, WS_2 and $MoSe_2$), MXenes (Ti_2C, Ti_3C_2, V_2C and Ti_2N) and derivatives [MXenes-X (X = OH, O, F)] that are combined with MoS_2 for the formation of 2D heterostructures. We have carefully checked the results with and without van der Waals correction (see Table S1 in Supplementary Information), and found that van der Waals interaction plays an important role in describing the structural and energetic properties. Different binding geometries have been carefully examined before we can obtain the ground-state configuration with the lowest total energy. In Table 1, we listed the lattice mismatch, equilibrium distance (d_{eq}), binding energy (E_b) between MoS_2 with one V_S and the 2D structure, as well as work function of the isolated 2D structure. We can see that MoS_2/graphene, MoS_2/*h*-BN and MoS_2/phosphorene have a relatively large d_{eq} around 3.4 Å with a small E_b of 0.18~0.20 eV/Mo, indicative of very weak noncovalent interaction. Bilayer TMDs, including MoS_2/MoS_2, MoS_2/WS_2 and $MoS_2/MoSe_2$, have d_{eq} around 3.25 Å with E_b of 0.20 eV/Mo. With functionalized MXene, however, d_{eq} reduces to 2.9, 2.8, and 2.35 Å for Ti_2C-O, Ti_2C-F and Ti_2C-OH, respectively. The calculated E_b between MoS_2 and Ti_2C-F/O is around 0.20 eV/Mo, which greatly increases to 0.40 eV/Mo between MoS_2 and Ti_2C-OH. On Ti_2C, d_{eq} surprisingly reduces to around 1.7 Å with a large E_b of 1.67 eV/Mo, suggesting extremely strong chemical bonding. Results on heterostructures with other MXenes, including Ti_3C_2, Ti_2N, V_2C and derivatives, are presented in Table S2 in Supplementary Information.

The interfacial electronic properties of these heterostructures can be analyzed by calculating the differential charge density and charge transfer between MoS_2 and 2D structures. Here, differential charge density, $\Delta\rho$, can be calculated by, $\Delta\rho = \rho_{total} - (\rho_{MoS2} + \rho_{2D})$, where ρ_{total}, ρ_{MoS2}, and ρ_{2D} are charge densities of the heterostructure, isolated MoS_2 and 2D structure, respectively. Figures 3 a–j show the differential charge density plots for different heterostructures. One can see that the number of differential charge and the area where charge density redistributes differ significantly for different systems. For MoS_2/graphene, MoS_2/*h*-BN and MoS_2/phosphorene (Figs. 3a–c), due to the very weak van der Waals interaction, essentially no charge density redistribution can be found except the V_S site, where a little differential charge spreads. For MoS_2/TMDs systems (Figs. 3d–f), we can see some charge accumulation at the interface area. In sharp contrast, significant differential charge density occurs around MoS_2 layer as well as the interface region in MoS_2/Ti_2C (Fig. 3g). Such drastic charge redistribution originates from the formation of strong chemical bonding between MoS_2 and Ti_2C. When MoS_2 is combined with functionalized MXenes, we found charge accumulation mainly at the interface (see Figs. 3h–j). Interestingly, for MoS_2/Ti_2C-OH, although the differential charge density is relatively small compared to that of MoS_2/Ti_2C, at V_S site, significant charge density redistribution can be obviously seen (Fig. 3h). Moreover, by careful examining the symmetry and shape of the differential charge density, we are able to identify the main features of Mo *d* orbitals, which play a crucial role in determining the electronic structures of the V_S site.

We also provide a quantitative assessment of the charge transfer from 2D structures to MoS_2 by using Bader charge analysis.[51] As shown in Fig. 3k, we found that MoS_2 in MoS_2/graphene, MoS_2/*h*-BN, MoS_2/phosphene and MoS_2/TMDs obtains a very small number of 0.01~0.02 electrons per formula unit (*e* per *f. u.*) of MoS_2, which increase to 0.09 *e* per *f. u.* for MoS_2/Ti_2C-OH, indicating that MoS_2 is *n*-type doped in these systems. For MoS_2/Ti_2C, the electrons transferred to MoS_2 increase by an order of

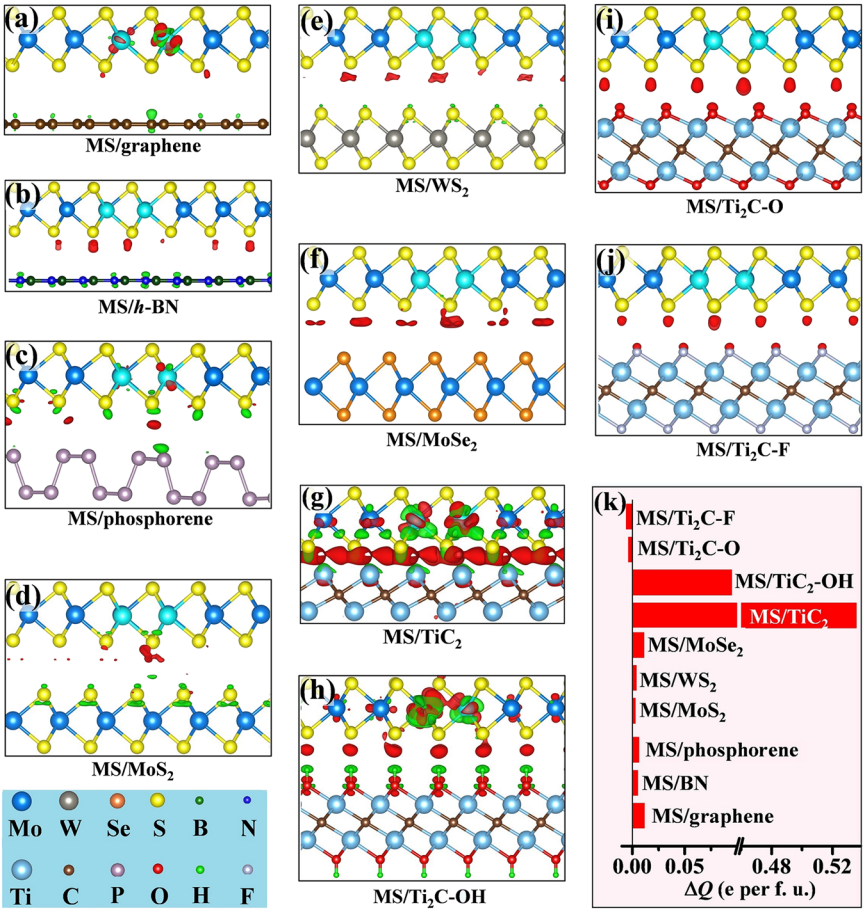

Fig. 3 **a**–**j** Differential charge density plots for different heterostructures of MoS_2 (MS) with one V_S and other 2D structures. Isosurface value in **a**–**f**, **i** and **j** is 0.0002 e/Å^3 and in **g**, **h** is 0.004 e/Å^3. Red color denotes electron accumulation and green represents electron depletion. **k** Quantitative charge transfer (ΔQ) from 2D structures to MoS_2

magnitude, reaching ~0.54 *e* per *f. u*. For MoS_2/Ti_2C-O and MoS_2/Ti_2C-F, our calculations show that MoS_2 loses 0.01~0.02 *e* per *f. u*., suggesting that MoS_2 becomes *p*-type doped. The direction of charge transfer is closely related to the work function (W_F) of the constituent materials that form the heterostructure. The calculated W_F of MoS_2 with one V_S is 5.25 eV, which is smaller than that of Ti_2C-O (5.6 eV) and Ti_2C-F (5.3 eV), but larger than that of other 2D structures (1.6~5.2 eV, see Table 1), which contributes to the opposite charge transfer and different types of doping in MoS_2. These analyses are in good accordance with the differential charge density presented above.

Next, we explored the electronic structures of V_S in these heterostructures that are expected to be influenced by interfacial coupling within the heterostructure. Figure 4 shows the PDOS projected onto *d* orbitals of Mo atoms at V_S site, for which we can see characteristic change of the defect states as well as the position of the highest occupied state compared with those of freestanding MoS_2 (Fig. 4a). For MoS_2/graphene, MoS_2/*h*-BN, MoS_2/phosphorene and MoS_2/TMDs (Figs. 4b–g), very little change can be observed due to the weak interaction. For MoS_2/Ti_2C, we found a striking overlap between S 3*p* and Ti 4*d* orbitals (not shown here) because of the strong binding, and the electronic states spread over the entire energy gap of pristine MoS_2, leaving MoS_2 in a metallic state (Fig. 4h). The lowest unoccupied state is located at −4.87 eV, 0.37 eV lower than V_{NHE}, indicating that this system may provide a promising alternative for atomic H adsorption. The binding of MoS_2 and Ti_2C-OH is weaker, for which we can still see the energy gap of MoS_2. Interestingly, the position of the lowest unoccupied state is located at −4.67, 0.17 eV lower than V_{NHE} (Fig. 4i), even more promising for H adsorption. For MoS_2/Ti_2C-O and MoS_2/Ti_2C-F, PDOS shown in Fig. 4j and k look similar to those in Figs. 4a–g, except that the defect states are obviously broadened.

Seeing the effective modulation of electronic properties of V_S in MoS_2, we now explore the possible engineering of ΔG_H by interfacial interaction within these heterostructures. Figure 5 displays the calculated ΔG_H for one V_S in freestanding and assembled MoS_2 in different heterostructures, with the optimized structures presented in Fig. S3 in Supplementary Information. As mentioned before, ΔG_H has a value of 0.226 eV for freestanding MoS_2, indicating that binding of atomic H is energetically unfavorable, leading to slow HER kinetics.[52] When assembled with other 2D structures, the value of ΔG_H varies. As shown in Fig. 5, for V_S in MoS_2/graphene, MoS_2/*h*-BN, MoS_2/phosphorene and MoS_2/TMDs (MoS_2, WS_2 and $MoSe_2$), ΔG_H was calculated to be 0.209, 0.225, 0.224, 0.226, 0.225, and 0.224 eV, respectively, almost the same to that of the freestanding case. This is in accordance with the electronic structure calculations showing that the PDOS of Mo *d* orbitals around V_S have little modifications (see Figs. 4b–g). Interestingly, for MoS_2/Ti_2C, ΔG_H greatly reduces to 0.048 eV, and for MoS_2/Ti_2C-OH, ΔG_H further decreases to 0.035 eV, which is very close to the optimal value of $\Delta G_H = 0$. This enhanced adsorption originates from the presence of unoccupied states located below V_{NHE}, which enhances the interaction with H *s* orbital (Fig. 4h, i). For the other two heterostructures, ΔG_H has values of 0.190 and 0.211 eV for MoS_2/Ti_2C-O and MoS_2/Ti_2C-F, respectively, a little bit smaller

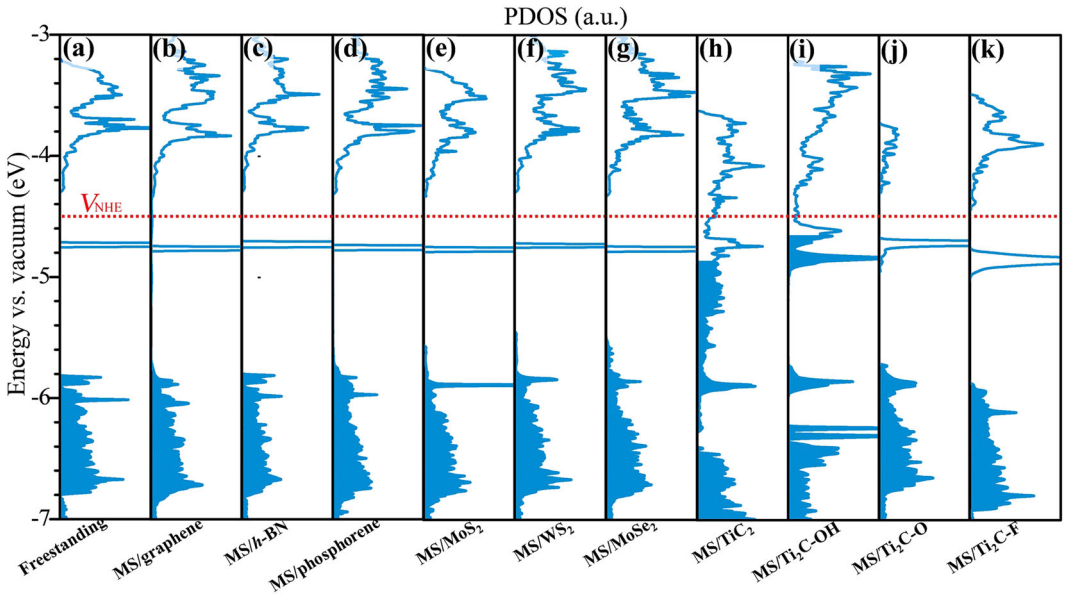

Fig. 4 PDOS projected onto *d* orbitals of exposed Mo atoms in **a** freestanding MoS_2 and **b**–**k** MoS_2 in different heterostructures. Empty and filled areas denote the unoccupied and occupied states, respectively. The energy location of V_{NHE} (4.5 eV *vs*. vacuum level) is denoted as the red dashed line

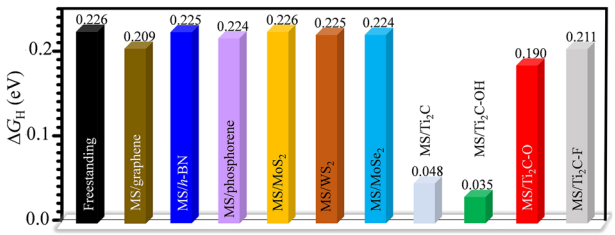

Fig. 5 Calculated ΔG_H of atomic H adsorption on V_S of freestanding and assembled MoS_2 in different heterostructures

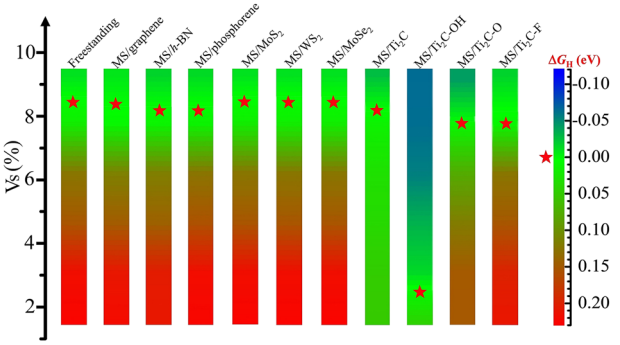

Fig. 6 Colored contour plot of ΔG_H on V_S of freestanding and assembled MoS_2 in different heterostructures with respect to increasing V_S%, from 1.52% to 9.38%. Color bar denotes the value of ΔG_H. Red star indicates the optimal value, $\Delta G_H = 0$

than ΔG_H for the freestanding case, which may be attributed to the broadened defect states (Figs. 4j, k).

We further expanded the concentration of V_S in these heterostructures by increasing the number of vacancies, from 1.56 to 9.38%, and explored the atomic H adsorption with the goal of achieving $\Delta G_H = 0$ so that the catalytic performance can be optimized. Figure 6 shows the energy contour of ΔG_H with respect to increasing V_S% for freestanding and assembled MoS_2 in different heterostructures. Clearly, in order to reach zero for ΔG_H, MoS_2/graphene, MoS_2/*h*-BN, MoS_2/ phosphorene and MoS_2/ TMDs need to have a high V_S% of over 8%. For MoS_2/Ti_2C, although ΔG_H has a small value of 0.048 eV at V_S of 1.56%, this value changes very slowly with respect to V_S%. Consequently, about 8% of V_S is needed for $\Delta G_H = 0$. This is due to the fact that MoS_2 has a complete metallic state when assembled with Ti_2C, and the electronic structures of V_S hardly change with increasing V_S%. The most interesting system is MoS_2/Ti_2C-OH, for which an optimal H adsorption ($\Delta G_H = 0$) can be obtained at a low V_S% of 2.5%. In this sense, Ti_2C-OH outperforms other 2D structures in tuning the interfacial interaction with MoS_2 and optimizing the atomic H adsorption.

We also studied the assembly of MoS_2 with a set of other MXenes, including Ti_3C_2, Ti_3C_2-O, Ti_3C_2-F, Ti_3C_2-OH, V_2C-OH, and Ti_2N-OH in together with the adsorption properties of H, with detailed results presented in Figs. S4-S7 in Supplementary Information. It was found in MoS_2/Ti_3C_2-OH, MoS_2/Ti_2N-OH and MoS_2/V_2C-OH, $\Delta G_H = 0$ can be achieved at V_S% of 2.75, 3.75, and 4.94% respectively, much lower that the V_S% needed for an optimal activity in freestanding MoS_2 (~9%). Furthermore, with appropriate interfacial interaction that benefits H adsorption, another advantage pertaining to MoS_2/MXene-OH assemblies lies in their unique structural properties, i.e., they have a weakly-bound layered nature with high porosity (Fig. 1), offering plenty of space for hydrogen absorption and escape, ideal for efficient water splitting.

It is noteworthy that most experimentally synthesized MXenes have a mixture of −OH, −O, and −F terminations.[38] Selection of functional groups, such as pure Ti_3C_2-OH and Ti_3C_2-O can be facilely made through an alkali-assisted hydrothermal method.[53] Moreover, as many MXenes are metallic,[54] which may greatly enhance carrier transport during electrocatalytic process, also beneficial for the overall HER activity. Therefore, our proposed approach shows the promise of using 2D heterostructures as high-performance catalyst for practical implementation.

To summarize, we have demonstrated the possibility of employing heterostructure assembly by integration of MoS_2 with 2D structures for HER. We show that among the typical 2D structures explored, MXene-OH is particularly interesting as a

constituent layer for MoS_2, for which an optimal $\Delta G_H = 0$ eV can be achieved at a low V_S% of ~2.5%. We reveal the critical role of interfacial interaction, which influences the characteristics of defect states induced by V_S, especially position and density of the lowest unoccupied state that determines the adsorption strength of atomic H. We highlight the features of porous structure, tunablity of electronic properties, as well as the rich alternatives for van der Waals assembly, rendering a feasible strategy to reach high catalytic activity on the basal plane of MoS_2. The fundamental principle is generally applicable to other 2D TMDs, thus providing an interesting approach for efficient hydrogen production. We believe that the combination of defect engineering with van der Waals assembly may further our ability to manipulate the physical properties of 2D systems with multi-functionalities.

METHODS

Periodic DFT calculations were performed with a plane-wave basis set as implemented in the Vienna ab initio simulation package,[55,56] using the projector augmented-wave method. For the exchange-correlation functional, we used the generalized gradient approximation in Perdew−Burke−Ernzerhof format with inclusion of van der Waals corrections (optPBE-vdW).[57–59] We have checked the calculation without van der Waals corrections, and the results are shown in Table S1. The energy cutoff for the plane-wave basis was set to 400 eV. Dipole corrections were applied in order to remove spurious dipole interactions between periodic images.[60]

The lattice constant of MoS_2 monolayer was calculated to be 3.21 Å, close to the experimental value of 3.16 Å.[61] 2D heterostructures were modeled by using a rectangular 4×8 supercell of MoS_2 on top of a 5×10 supercell of graphene, *h*-BN and black phosphorene, a 4×8 supercell of TMDs (MoS_2, WS_2 and $MoSe_2$), a 4×8 supercell of MXenes (Ti_2C, Ti_3C_2, V_2C and Ti_2N) and their functionalized derivatives (MXenes-X, X = OH, O, F). As a result, the lattice mismatch between MoS_2 and 2D structure lies within −4.0~4.50% (see Table 1 and S2). A $6 \times 6 \times 1$ *k*-point mesh was used for structural optimization and a $9 \times 9 \times 1$ *k*-point mesh for energy and electronic structure calculation. All atoms were fully relaxed until the forces on each atom were smaller than 0.01 eV/Å. A vacuum region of over 20 Å was used to eliminate the interaction between neighboring slabs. To explore the influence of strain existed in heterostructures, we also constructed models by rotating the relative orientation of 2D structures with respect to MoS_2 (see Fig. S8), the lattice mismatch can be reduced (Table S3). By comparing the work function of isolated 2D structures and charge transfer of heterostructures based on the two models, we found that the strain effects on charge transfer is very limited (see Table S3 and Fig. S9).

V_S was created by removing S atoms from the basal plane of MoS_2, where its concentration, V_S%, is defined as the number of removed S atoms divided by the total number of S atoms in the system. Within the supercell constructed above, one V_S in each system corresponds to 1.56%, and V_S% of more vacancies can be calculated accordingly. In experiments, Vs was shown to be dispersed as single point defect on the basal plane of MoS_2.[23,24,62] Therefore, we constructed V_S of high concentrations that are uniformly distributed on MoS_2 (see Fig. S1). This is also desirable for maximizing the exposed active sites. Within each heterostructure, the binding energy (E_b) between MoS_2 and other 2D structures can be calculated by, $E_b = -[E_{total} - (E_{MoS2} + E_{2D}]/n$, where E_{total}, E_{MoS2}, and E_{2D} represent the total energy of the heterostructure, separated MoS_2 and 2D structure, respectively. *n* is the number of Mo atoms.

The free energy of atomic H adsorption, ΔG_H, is defined as, $\Delta G_H = \Delta E_H + \Delta E_{ZPE} - T\Delta S$,[4,15,30] where ΔE_H is the adsorption energy and can be calculated by, $\Delta E_H = E_{H@catalyst} - (E_{catalyst} + \frac{1}{2}E_{H2})$, where $E_{H@catalyst}$, $E_{catalyst}$, and E_{H2} refer to the total energy of H atom adsorbed on the catalyst surface, catalyst without H adsorption and H_2 in gas phase, respectively. ΔE_{ZPE} can be calculated by, $\Delta E_{ZPE} = E_{ZPE}(*H) - \frac{1}{2}E_{ZPE}(H_2)$, where $E_{ZPE}(*H)$ and $E_{ZPE}(H_2)$ are the zero-point energy of H in the adsorbed state and H_2 in gas phase, respectively. ΔS is obtained by, $\Delta S = S(*H) - \frac{1}{2}S(H_2)$, where $S(*H)$ and $S(H_2)$ represent the entropy of one adsorbed H atom and H_2 in gas phase. As the entropy contribution from the adsorbed H, $S(*H)$, is very small and can be neglected,[4,30] ΔS can be estimated as, $\Delta S \cong -\frac{1}{2}S(H_2)$. $E_{ZPE}(H_2)$ and $S(H_2)$ can be taken from standard molecular tables, that is, $E_{ZPE}(H_2) = 0.27$ eV and $S(H_2) = 131.6$ J/K mol.[63] Therefore, at standard conditions (1 bar, 300 K), ΔG_H is simplified as, $\Delta G_H = \Delta E_H + E_{ZPE}(*H) + 0.07$ eV. For MoS_2 and related systems, previous studies[4,17,64–67] showed that $E_{ZPE}(*H) \approx 0.22$ eV, regardless of the adsorption site. We examined the effect of underlying 2D structures on $E_{ZPE}(*H)$, and found that the change of $E_{ZPE}(*H)$ is less than 0.01 eV. Therefore, we used $E_{ZPE}(*H) = 0.22$ eV for the constructed heterostructures, so that ΔG_H can be expressed as, $\Delta G_H = \Delta E_H + 0.29$ eV. We did not include solvent effect on ΔG_H due to the hydrophobic nature of MoS_2,[68] which was also neglected in literatures.[4,15,17,21,64–67]

DATA AVAILABILITY

The authors declare that all data supporting the findings of this study are available within the paper and its supplementary information.

ACKNOWLEDGEMENTS

This work was supported by the National Natural Science Foundation of China (11674042), the Science Challenge Project (TZ2018004), the Fundamental Research Funds for the Central Universities (106112016CDJXY120001) and the Thousand Youth Talents Program of China.

AUTHOR CONTRIBUTIONS

F.L. performed the DFT calculations with help from W.K., H.J., W.Z., Y.C., X.L., Y.Z., and L.Q. All authors contributed to the discussion. F.L. and M.Z. wrote the manuscript. M. Z. conceived the idea and designed the project.

ADDITIONAL INFORMATION

Supplementary information accompanies the paper on the *npj Computational Materials* website (https://doi.org/10.1038/s41524-019-0161-8).

Competing interests: The authors declare no competing interests.

Publisher's note: Springer Nature remains neutral with regard to jurisdictional claims in published maps and institutional affiliations.

REFERENCES

1. Greeley, J., Jaramillo, T. F., Bonde, J., Chorkendorff, I. B. & Nørskov, J. K. Computational high-throughput screening of electrocatalytic materials for hydrogen evolution. *Nat. Mater.* **5**, 909–913 (2006).
2. Merki, D. & Hu, X. Recent developments of molybdenum and tungsten sulfides as hydrogen evolution catalysts. *Energy Environ. Sci.* **4**, 3878–3888 (2011).
3. Ling, F. L. et al. Electric field tuned MoS_2/metal interface for hydrogen evolution catalyst from first-principles investigations. *Nanotechnology* **29**, 03LT01 (2017).
4. Hinnemann, B. et al. Biomimetic hydrogen evolution: MoS_2 nanoparticles as catalyst for hydrogen evolution. *J. Am. Chem. Soc.* **127**, 5308–5309 (2005).
5. Jaramillo, T. F. et al. Identification of active edge sites for electrochemical H_2 evolution from MoS_2 nanocatalysts. *Science* **317**, 100–102 (2007).
6. Ling, F. et al. Optimizing edges and defects of supported MoS_2 catalyst for hydrogen evolution via external electric field. *Phys. Chem. Chem. Phys.* **20**, 26083–26090 (2018).
7. Li, Y. et al. MoS_2 nanoparticles grown on graphene: an advanced catalyst for the hydrogen evolution reaction. *J. Am. Chem. Soc.* **133**, 7296–7299 (2011).
8. Kong, D. et al. Synthesis of MoS_2 and $MoSe_2$ films with vertically aligned layers. *Nano. Lett.* **13**, 1341–1347 (2013).
9. Chen, Z. et al. Core-shell MoO_3-MoS_2 nanowires for hydrogen evolution: a functional design for electrocatalytic materials. *Nano. Lett.* **11**, 4168–4175 (2011).
10. Kibsgaard, J., Chen, Z., Reinecke, B. N. & Jaramillo, T. F. Engineering the surface structure of MoS_2 to preferentially expose active edge sites for electrocatalysis. *Nat. Mater.* **11**, 963–969 (2012).
11. Hou, Y. et al. Bioinspired molecular co-catalysts bonded to a silicon photocathode for solar hydrogen evolution. *Nat. Mater.* **10**, 434–438 (2011).
12. Merki, D., Vrubel, H., Rovelli, L., Fierro, S. & Hu, X. Fe, Co, and Ni ions promote the catalytic activity of amorphous molybdenum sulfide films for hydrogen evolution. *Chem. Sci.* **3**, 2515–2525 (2012).
13. Shi, Y. et al. Energy level engineering of MoS_2 by transition-metal doping for accelerating hydrogen evolution reaction. *J. Am. Chem. Soc.* **139**, 15479–15485 (2017).
14. Liu, G. et al. MoS_2 monolayer catalyst doped with isolated Co atoms for the hydrodeoxygenation reaction. *Nat. Chem.* **9**, 810–816 (2017).

15. Li, H. et al. Activating and optimizing MoS_2 basal planes for hydrogen evolution through the formation of strained sulphur vacancies. *Nat. Mater.* **15**, 48–53 (2016).
16. Ambrosi, A., Sofer, Z. & Pumera, M. 2H → 1T phase transition and hydrogen evolution activity of MoS_2, $MoSe_2$, WS_2 and WSe_2 strongly depends on the MX_2 composition. *Chem. Commun.* **51**, 8450–8453 (2015).
17. Gao, G. et al. Charge mediated semiconducting-to-metallic phase transition in molybdenum disulphide monolayer and hydrogen evolution reaction in new 1T′ phase. *J. Phys. Chem. C.* **119**, 13124–13128 (2015).
18. Tang, Q. & Jiang, D. Mechanism of hydrogen evolution reaction on 1T-MoS_2 from first principles. *ACS Catal.* **6**, 4953–4961 (2016).
19. Lin, Y. C., Dumcenco, D. O., Huang, Y. S. & Suenaga, K. Atomic mechanism of the semiconducting-to-metallic phase transition in single-layered MoS_2. *Nat. Nanotechnol.* **9**, 391–396 (2014).
20. Eda, G. et al. Photoluminescence from chemically exfoliated MoS_2. *Nano. Lett.* **11**, 5111–5116 (2011).
21. Ouyang, Y. et al. Activating inert basal planes of MoS_2 for hydrogen evolution reaction through the formation of different intrinsic defects. *Chem. Mater.* **28**, 4390–4396 (2016).
22. Lin, S. H. & Kuo, J. L. Activating and tuning basal planes of MoO_2, MoS_2, and $MoSe_2$ for hydrogen evolution reaction. *J. Phys. Chem. C.* **17**, 29305–29310 (2015).
23. Hong, J. et al. Exploring atomic defects in molybdenum disulphide monolayers. *Nat. Commun.* **6**, 6293 (2015).
24. Li, G. et al. All the catalytic active sites of MoS_2 for hydrogen evolution. *J. Am. Chem. Soc.* **138**, 16632–16638 (2016).
25. Qiu, H. et al. Hopping transport through defect-induced localized states in molybdenum disulphide. *Nat. Commun.* **4**, 2642 (2013).
26. Voiry, D. et al. The role of electronic coupling between substrate and 2D MoS_2 nanosheets in electrocatalytic production of hydrogen. *Nat. Mater.* **15**, 1003–1009 (2016).
27. Ye, G. et al. Defects engineered monolayer MoS_2 for improved hydrogen evolution reaction. *Nano. Lett.* **16**, 1097–1103 (2016).
28. Tsai, C. et al. Electrochemical generation of sulfur vacancies in the basal plane of MoS_2 for hydrogen evolution. *Nat. Commun.* **8**, 15113 (2017).
29. Gennero de Chialvo, M. R. & Chialvo, A. C. Hydrogen evolution reaction: Analysis of the Volmer-Heyrovsky-Tafel mechanism with a generalized adsorption model. *J. Electroanal. Chem.* **372**, 209–223 (1994).
30. Nørskov, J. K. et al. Trends in the exchange current for hydrogen evolution. *J. Electrochem. Soc.* **152**, J23–J26 (2005).
31. Novoselov, K. S., Mishchenko, A., Carvalho, A. & Castro Neto, A. H. 2D materials and van der Waals heterostructures. *Science* **353**, aac9439 (2016).
32. Deng, D. et al. Catalysis with two-dimensional materials and their heterostructures. *Nat. Nanotech.* **11**, 218–230 (2016).
33. Gao, M. R. et al. An efficient molybdenum disulfide/cobalt diselenide hybrid catalyst for electrochemical hydrogen generation. *Nat. Commun.* **6**, 5982 (2015).
34. Jariwala, D., Marks, T. J. & Hersam, M. C. Mixed-dimensional van der Waals heterostructures. *Nat. Mater.* **16**, 170–181 (2017).
35. Liu, Q. et al. Electron-doped 1T-MoS_2 via interface engineering for enhanced electrocatalytic hydrogen evolution. *Chem. Mater.* **29**, 4738–4744 (2017).
36. He, R. et al. Molybdenum disulfide-black phosphorus hybrid nanosheets as a superior catalyst for electrochemical hydrogen evolution. *Nano. Lett.* **17**, 4311–4316 (2017).
37. Voiry, D. et al. Conducting MoS_2 nanosheets as catalysts for hydrogen evolution reaction. *Nano. Lett.* **13**, 6222–6227 (2013).
38. Anasori, B., Lukatskaya, M. R. & Gogotsi, Y. 2D metal carbides and nitrides (MXenes) for energy storage. *Nat. Rev. Mater.* **2**, 16098 (2017).
39. Tsai, C., Chan, K., Nørskov, J. K. & Abild-Pedersen, F. Theoretical insights into the hydrogen evolution activity of layered transition metal dichalcogenides. *Surf. Sci.* **640**, 133–140 (2015).
40. Wang, J. et al. The mechanism of hydrogen adsorption on transition metal dichalcogenides as hydrogen evolution reaction catalyst. *Phys. Chem. Chem. Phys.* **19**, 10125–10132 (2017).
41. Liu, Y. et al. Self-optimizing, highly surface-active layered metal dichalcogenide catalysts for hydrogen evolution. *Nat. Energy* **2**, 17127 (2017).
42. Miwa, J. A. et al. Van der Waals epitaxy of two-dimensional MoS_2-graphene heterostructures in ultrahigh vacuum. *ACS Nano* **9**, 6502–6510 (2015).
43. Shi, Y. et al. Van der Waals epitaxy of MoS_2 layers using graphene as growth templates. *Nano. Lett.* **12**, 2784–2791 (2012).
44. Yu, L. et al. Graphene/MoS_2 hybrid technology for large-scale two-dimensional electronics. *Nano. Lett.* **14**, 3055–3063 (2014).
45. Yan, A. et al. Direct growth of single- and few-layer MoS_2 on *h*-BN with preferred relative rotation angles. *Nano. Lett.* **15**, 6324–6331 (2015).
46. Wang, S., Wang, X. & Warner, J. H. All chemical vapor deposition growth of MoS_2: *h*-BN vertical van der Waals heterostructures. *ACS Nano* **9**, 5246–5254 (2015).
47. Deng, Y. et al. Black phosphorus–monolayer MoS_2 van der Waals heterojunction *p–n* diode. *ACS Nano* **8**, 8292–8299 (2014).
48. Tongay, S. et al. Tuning interlayer coupling in large-area heterostructures with CVD-grown MoS_2 and WS_2 monolayers. *Nano. Lett.* **14**, 31853190 (2014).
49. Ceballos, F., Bellus, M. Z., Chiu, H. Y. & Zhao, H. Ultrafast charge separation and indirect exciton formation in a MoS_2-$MoSe_2$ van der Waals heterostructure. *ACS Nano* **8**, 12717–12724 (2014).
50. Gan, L. Y., Zhao, Y. J., Huang, D. & Schwingenschlögl, U. First-principles analysis of MoS_2/Ti_2C and MoS_2/Ti_2CY_2 (Y = F and OH) all-2D semiconductor/metal contacts. *Phys. Rev. B* **87**, 245307 (2013).
51. Henkelman, G., Arnaldsson, A. & Jonsson, H. A fast and robust algorithm for Bader decomposition of charge density. *Comput. Mater. Sci.* **36**, 354–360 (2006).
52. Shu, H., Zhou, D., Li, F., Cao, D. & Chen, X. Defect engineering in $MoSe_2$ for hydrogen evolution reaction: from point defects to edges. *ACS Appl. Mater. Interfaces* **9**, 42688–42698 (2017).
53. Li, T. et al. Fluorine-free synthesis of high-purity $Ti_3C_2T_x$ (T = OH, O) *via* alkali treatment. *Angew. Chem. Int. Ed.* **57**, 1–6 (2018).
54. Khazaei, M. et al. Nearly free electron states in MXenes. *Phys. Rev. B* **93**, 205125 (2016).
55. Kresse, G. & Furthmuller, J. Efficient iterative schemes for ab initio total-energy calculations using a plane-wave basis set. *Phys. Rev. B* **54**, 11169–11186 (1996).
56. Kresse, G. & Furthmuller, J. Efficiency of ab-initio total energy calculations for metals and semiconductors using a plane-wave basis set. *Comp. Mater. Sci.* **6**, 15–50 (1996).
57. Perdew, J. P., Burke, K. & Ernzerhof, M. Generalized gradient approximation made simple. *Phys. Rev. Lett.* **78**, 1396–1396 (1997).
58. Kresse, G. & Joubert, D. From ultrasoft pseudopotentials to the projector augmented-wave method. *Phys. Rev. B* **59**, 1758–1775 (1999).
59. Klimes, J., Bowler, D. R. & Michaelides, A. Van der Waals density functionals applied to solids. *Phys. Rev. B* **83**, 195131 (2011).
60. Makov, G. & Payne, M. C. Periodic boundary conditions in ab initio calculations. *Phys. Rev. B* **51**, 4014–4022 (1995).
61. Raybaud, P., Hafner, J., Kresse, G., Kasztelan, S. & Toulhoat, H. Structure, energetics, and electronic properties of the surface of a promoted MoS_2 catalyst: an ab initio local density functional study. *J. Catal.* **190**, 128–143 (2000).
62. Li, H. et al. Kinetic study of hydrogen evolution reaction over strained MoS_2 with sulfur vacancies using scanning electrochemical microscopy. *J. Am. Chem. Soc.* **138**, 5123–5129 (2016).
63. Atkins, P. W. *Physical Chemistry* 6th edn, 485, 866–867, 925–927, 942 (Oxford University Press, Oxford, UK, 1998).
64. Chou, S. S. et al. Understanding catalysis in a multiphasic two-dimensional transition metal dichalcogenide. *Nat. Commun.* **6**, 8311 (2015).
65. Lazar, P. & Otyepka, M. Role of the edge properties in the hydrogen evolution reaction on MoS_2. *Chem. Eur. J.* **23**, 4863–4869 (2017).
66. Bruix, A., Lauritsen, J. V. & Hamme, B. Effects of particle size and edge structure on the electronic structure, spectroscopic features, and chemical properties of Au (111)-supported MoS_2 nanoparticles. *Faraday Discuss.* **188**, 323–343 (2016).
67. Ling, C. Y. et al. Template-grown MoS_2 nanowires catalyze the hydrogen evolution reaction: ultralow kinetic barriers with high active site density. *ACS Catal.* **7**, 5097–5102 (2017).
68. Gaur, A. P. S. et al. Surface energy engineering for tunable wettability through controlled synthesis of MoS_2. *Nano. Lett.* **14**, 4314–4321 (2014).

Open Access This article is licensed under a Creative Commons Attribution 4.0 International License, which permits use, sharing, adaptation, distribution and reproduction in any medium or format, as long as you give appropriate credit to the original author(s) and the source, provide a link to the Creative Commons license, and indicate if changes were made. The images or other third party material in this article are included in the article's Creative Commons license, unless indicated otherwise in a credit line to the material. If material is not included in the article's Creative Commons license and your intended use is not permitted by statutory regulation or exceeds the permitted use, you will need to obtain permission directly from the copyright holder. To view a copy of this license, visit http://creativecommons.org/licenses/by/4.0/.

© The Author(s) 2019